FIRST RESULTS FROM PHAROS, THE NEW CHOPPER SPECTROMETER AT LANSCE

B. J. Olivier, J. P. Sandoval, P. S. Lysaght, M. Nutter and R. A. Robinson
LANSCE, Los Alamos National Laboratory, Los Alamos, NM 87545, USA.

Abstract

In this article we present the first experimental measurements obtained on PHAROS during the 1992 run cycle at LANSCE. These are data on the phasing of the choppers relative to the accelerator system along with the consequent neutronic resolution, data on the real-space position resolution of the main detectors, a white-beam nickel powder calibration, and our first inelastic scattering measurement made on TiH_2 with an incident energy of 300meV. The characteristic features of the new chopper spectrometer PHAROS, designed for low-angle inelastic neutron scattering and neutron Brillouin scattering, are described elsewhere in these proceedings[1].

1. Phasing of the High Speed Chopper Relative to the LAMPF/PSR Accelerator System

As stated in Ref. 1, we have developed a scheme whereby our fast chopper system electronics triggers both the firing of the main LAMPF linear accelerator and the extraction of protons from the proton storage ring. This phasing of the fast chopper allows one to select an incident neutron energy, E_i, on the sample. Figure 1(a) shows the signal from the magnetic pickup of the fast chopper, measured with respect to the arrival time of protons on the target. A vetoing system has been employed for uncertainties outside a 10μs time window, and a vetoing rate less than 0.5% was observed. We expect a phase error somewhat greater than the 0.37μs which corresponds to the circumference of the storage ring. Furthermore, since the chopper must accelerate or decelerate to follow a smoothed electrical-supply line frequency, there will be additional dephasing. Our data show a phasing error of approximately 1.1μs FWHM, which is less than the moderation time at all relevant neutron energies.

Figure 1(b) shows the signal from the beam monitor directly down stream from the fast chopper (186mm behind). The data in (b) were fit to $c(t) = A \exp(-(t-t_o)^2/2\sigma^2_{meas})$ where $\sigma^2_{meas} = \sigma^2_{mon} + \sigma^2_t$. σ_{mon} results from the finite monitor thickness while σ_t is the true energy resolution in time units. After correcting for the width (25.4mm) of the BF_3 monitor we find $\sigma_t = 1.46 \pm 0.05$μs (FWHM = 3.44 ± 0.12μs). This value is in good agreement with the calculated resolution of $\sigma_{calc} = 1.32$μs.

2. Position Resolution of Main Detectors

The main detector bank consists of forty, 0.914m active length, 10atm linear position-sensitive ^3He detectors. The detector array covers $1.2m^2$ in the forward scattering direction. A mapping of the detector array is shown in Fig. 2. The spectrometer design specifies 2.5cm spatial resolution along the length of each of these tubes. To investigate the spatial resolution, we have performed experiments in which the detectors were completely covered with absorbing material, except for 2 widely separated 5-cm slots, as shown in Figure 3(a). the results for a white beam, scattered from an isotropic (hydrogenated) scatterer are shown in Figure 3(b). Since the absorbing mask used was cadmium, we have chosen to integrate the incident spectrum only over energies where we are sure the cadmium is black i.e. from $10 < E_i < 150$meV. The peaks in (b) were fit to $c(y) = A \exp(-(y-y_o)^2/2\sigma^2_{meas})$ where $\sigma^2_{meas} = \sigma^2_{det} + \sigma^2_{cad}$. σ_{cad} results from the 5cm wide apertures while σ_{det} represents the true intrinsic detector resolution. The measured resolution is given by a FWHM of 9.9cm, which after correcting for the size of the 5cm aperture gives an intrinsic detector resolution of approximately 8.9cm FWHM. Since October 1992, we have been working on improving this

resolution by increasing the detector gain, adjusting the discrimination levels in the channel logic boards and load matching the pre-amp to detector couplings.

3. White-Beam diffraction measurements

In order to investigate the position sensitivity and to calibrate the scattering angle scale on the detector plane, we performed total diffraction measurements on a standard nickel powder sample. The results are shown in Figure 4. The ordinate represents time-of-flight measured in a given pixel of the detector plane. The low-order nickel reflections have been indexed as shown. Each band along the abscissa represents a particular detector (a certain value of x measured horizontally away from the straight-through beam), with the 32 pixels (the y-variation in the vertical direction along the length of each detector) represented within each band. The crescent shaped Bragg reflections, merely reflect the Debye-Scherrer cones projected onto particular detectors. For any given Bragg reflection, the observed time is a minimum at the center of each detector, because the Bragg angle is a minimum there. For detectors closer to the straight-through beam, that minimum time also decreases with scattering angle ϕ.

4. Inelastic Measurements

Figure 5 shows our first inelastic scattering measurement from a 24g TiH_2 sample[2], using a nominal incident energy of 300meV. The calibration simply used the rigid body distances in the spectrometer, and the nominal timing of the fast chopper electronics. The elastic energy is close to zero indicating an incident energy of 304.2 ± 0.15meV. Inelastic features around 140 meV are indicative of the Einstein mode that has been previously studied elsewhere[2]. The observed width is significantly greater than the spectrometer resolution and the structure is due to dispersion. It is worth noting that the relative intensities of the two peaks are different from those reported in reference[2]. In our data, the lower energy transfer peak is more intense. This is a Q-dependent effect and in a similar system, ZrH_2, the inelastic structure at low-Q is similar to ours[3].

Note, however, that the observed elastic resolution (4%) for this measurement is significantly worse than the calculated (1.7%). We can account for this discrepancy in two ways. First, the trigger to the proton-storage ring was not connected. This was realized because our phasing to the accelerator was only 4.5μs FWHM, rather than the 1.0μs shown in Figure 1(a). Even after accounting for the phasing error, however, the resolution is still poorer than expected. We believe that this additional width is caused by the leakage of neutrons around the outside of the slit package of the fast chopper. The slit package has the same nominal size (5 x 7.5 cm^2) as the final boron composite aperture before the fast chopper, and we had found it necessary to place slightly smaller apertures before and after the fast chopper. When the 300meV chopper was installed, and these measurements taken, these apertures were inadvertently left out. Support for this view can be found in the strange shape of the elastic line, which is quite sharp at the center but with significant wings on either side.

5. Conclusions

In conclusion, we have fully operated all aspects of the spectrometer simultaneously: fast chopper, T-zero chopper, vacuum system with vacuum window, position-sensitive detectors and beam monitors. Satisfactory results have been obtained and with resolution improvements currently being made, we believe PHAROS will be ready for original experiments during 1993.

Acknowledgments

This work was supported in part by the Division of Basic Energy Sciences of the US Department of Energy.

References

1. R. A. Robinson, M. Nutter, R. L. Ricketts, E. Larson, J. P. Sandoval, P. Lysaght and B. J. Olivier, in these proceedings.
2. C. Korn and D. Zamir, *J. Phys. Chem. Solids*, **34**, 725 (1973).
3. J. G. Couch, O. K. Harling and L. C. Clune, *Phys. Rev.* **B4**, 2675 (1971).

Figure Captions

Figure 1. Plots of (a) the magnetic pick-up signal for the fast Fermi chopper (18m from the source), (b) signal in a 2.54cm-thick BF_3 beam monitor 0.186m downstream from the fast chopper.

Figure 2. Schematic of the PHAROS detector map to be used during the 1993 beam cycle at LANSCE. The gray scale gives the scattering angle spread.

Figure 3. Plots of intensity versus length along a linear position-sensitive detector. (a) shows the experimental setup, in which the detector is illuminated through two 5cm wide apertures. (b) shows in-beam results from October 1992. The spectra were summed over the energy range $10 < E_i < 150$meV.

Figure 4. Plots of intensity versus x, y, and t as measured in a few detectors on PHAROS. The fast chopper was removed in this measurement and the sample was 38g of nickel powder. The low-order reflections are indexed on the left hand side of the figure. The vertical axis represents observed time-of-flight in each pixel, while the horizontal axis represents both the x and y variations in the detector. The fine variation (32 pixels) is along the length (y) of each detector, while each band represents an individual tube (x-variation).

Figure 5. Plot of inelastically scattered intensity from TiH_2, using an incident energy of 300meV. (a) includes the elastic scattering while (b) focuses on the inelastic structure. The data in (b) show an order of magnitude increase in the signal over the background.

Fig.1

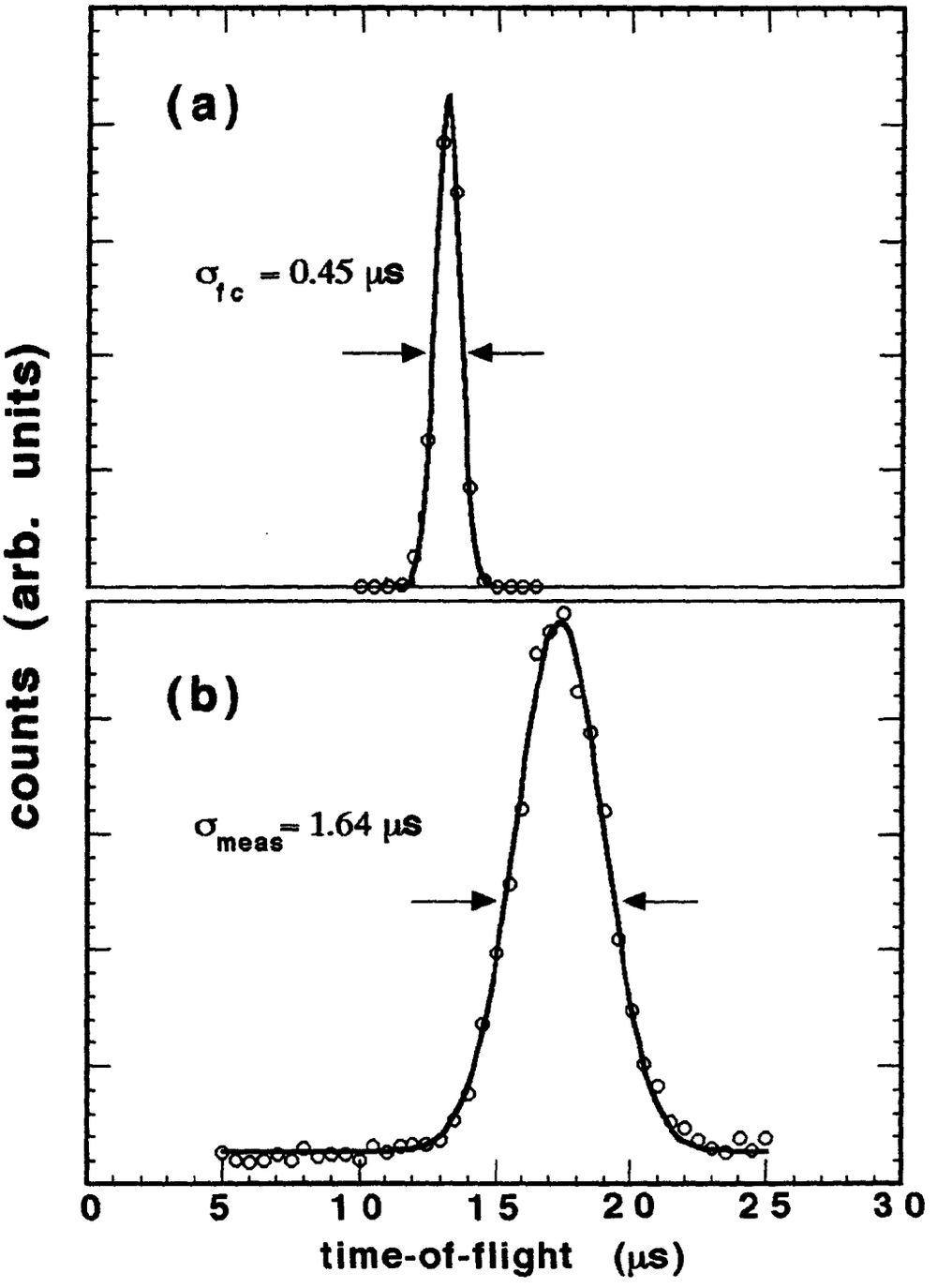
(a)
σ_{fc} = 0.45 μs
(b)
σ_{meas} = 1.64 μs
counts (arb. units)
0
5
10
15
20
25
30
time-of-flight (μs)

Fig.2

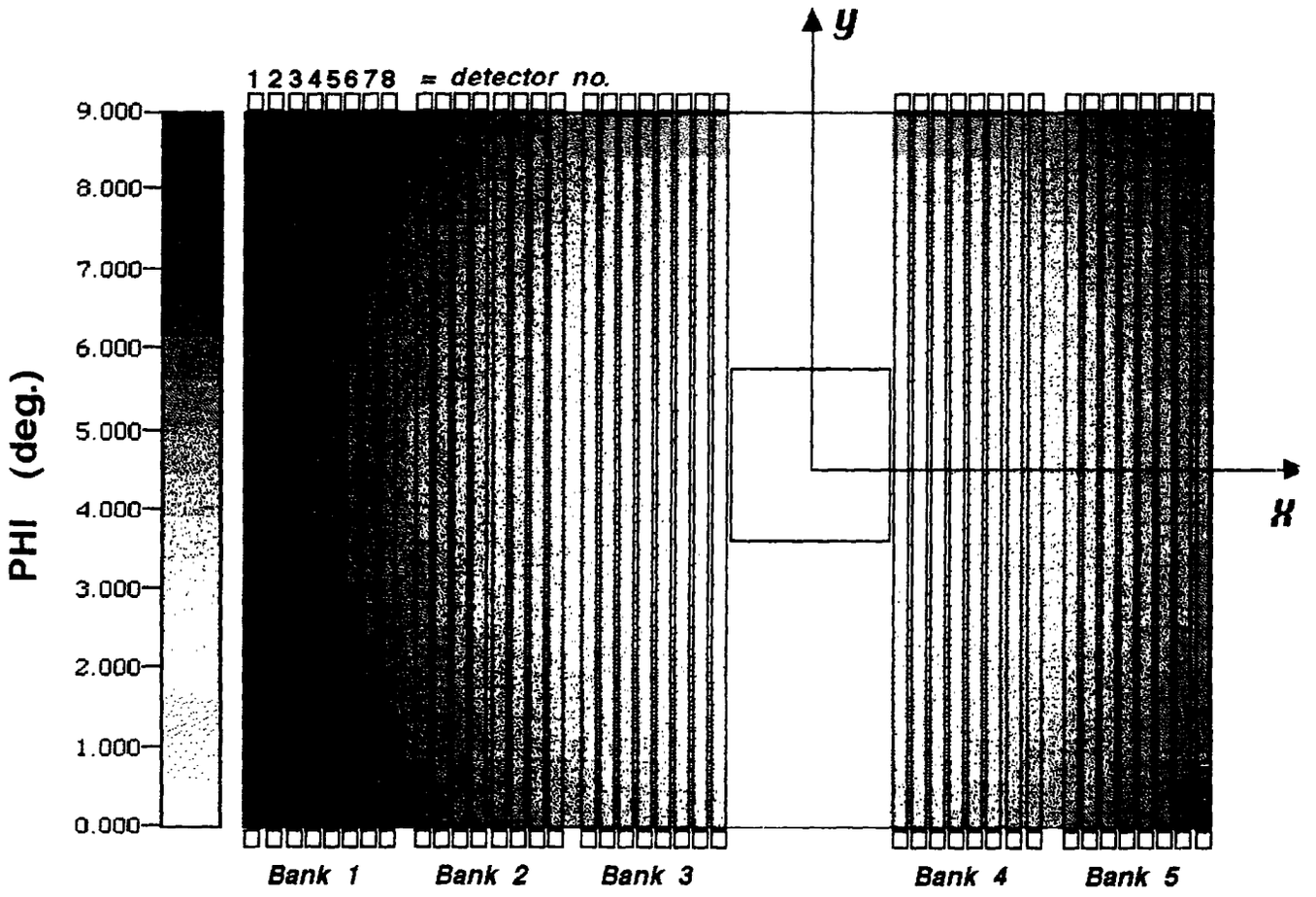
y
1 2 3 4 5 6 7 8 = detector no.
9.000
8.000
7.000
6.000
5.000
4.000
3.000
2.000
1.000
0.000
PHI (deg.)
x
Bank 1
Bank 2
Bank 3
Bank 4
Bank 5

Fig.3

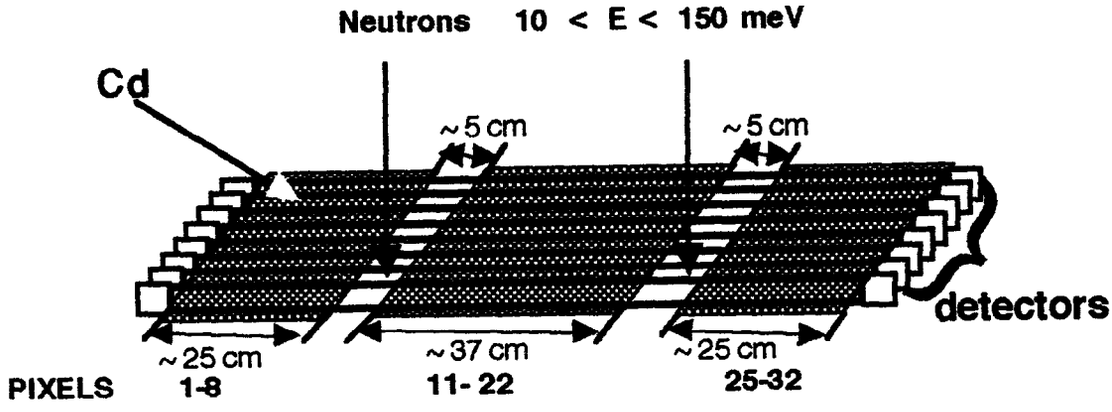
Neutrons 10 < E < 150 meV
Cd
~5 cm
~5 cm
detectors
~25 cm
~37 cm
~25 cm
PIXELS 1-8
11-22
25-32

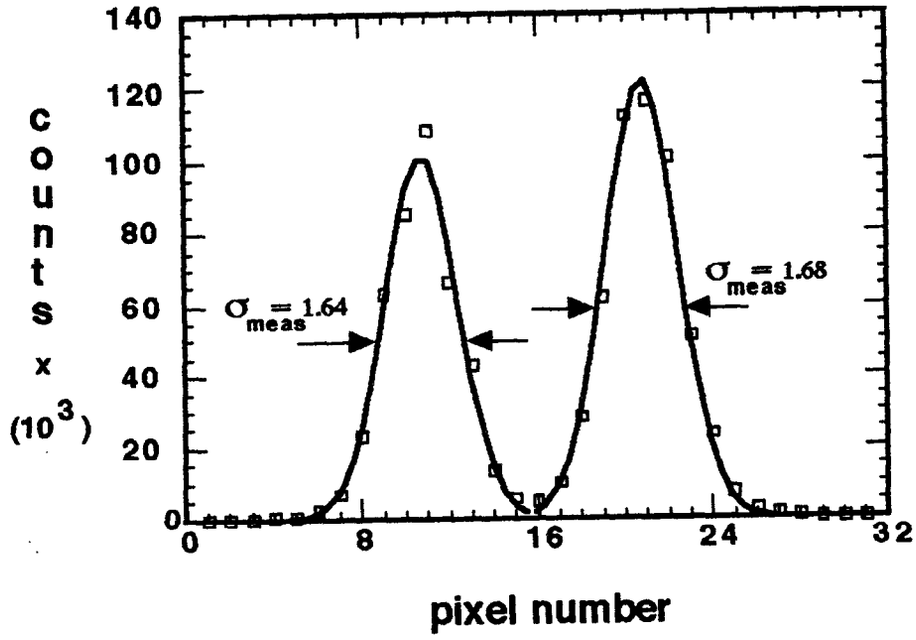
140
120
100
80
60
40
20
0
counts x (10^3)
σ meas = 1.64
σ meas = 1.68
0
8
16
24
32
pixel number

Fig.4

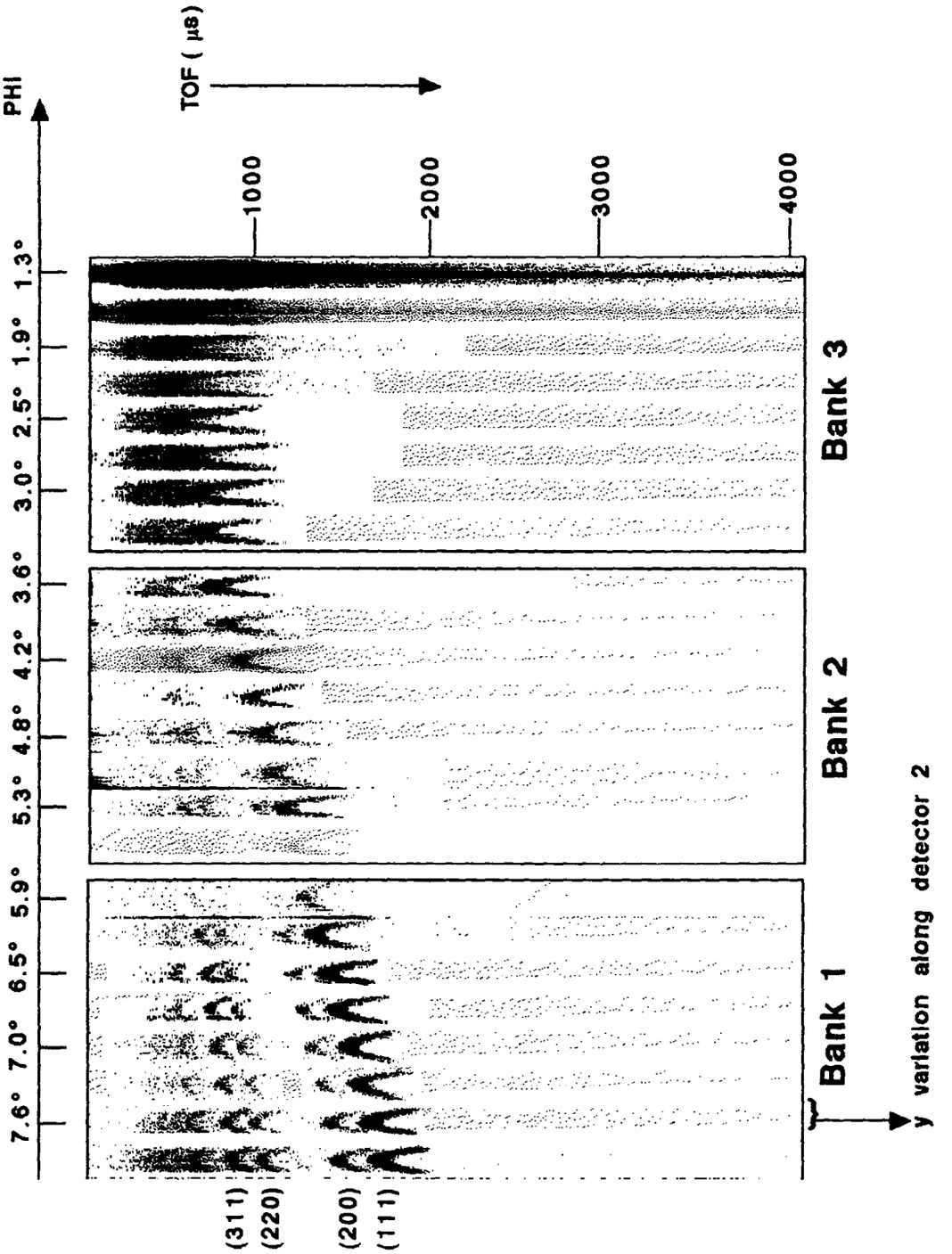
TOF (μs)
1000
2000
3000
4000
PHI
1.3°
1.9°
2.5°
3.0°
3.6°
4.2°
4.8°
5.3°
5.9°
6.5°
7.0°
7.6°
Bank 3
Bank 2
Bank 1
y variation along detector 2
(311)
(220)
(200)
(111)

Fig.5

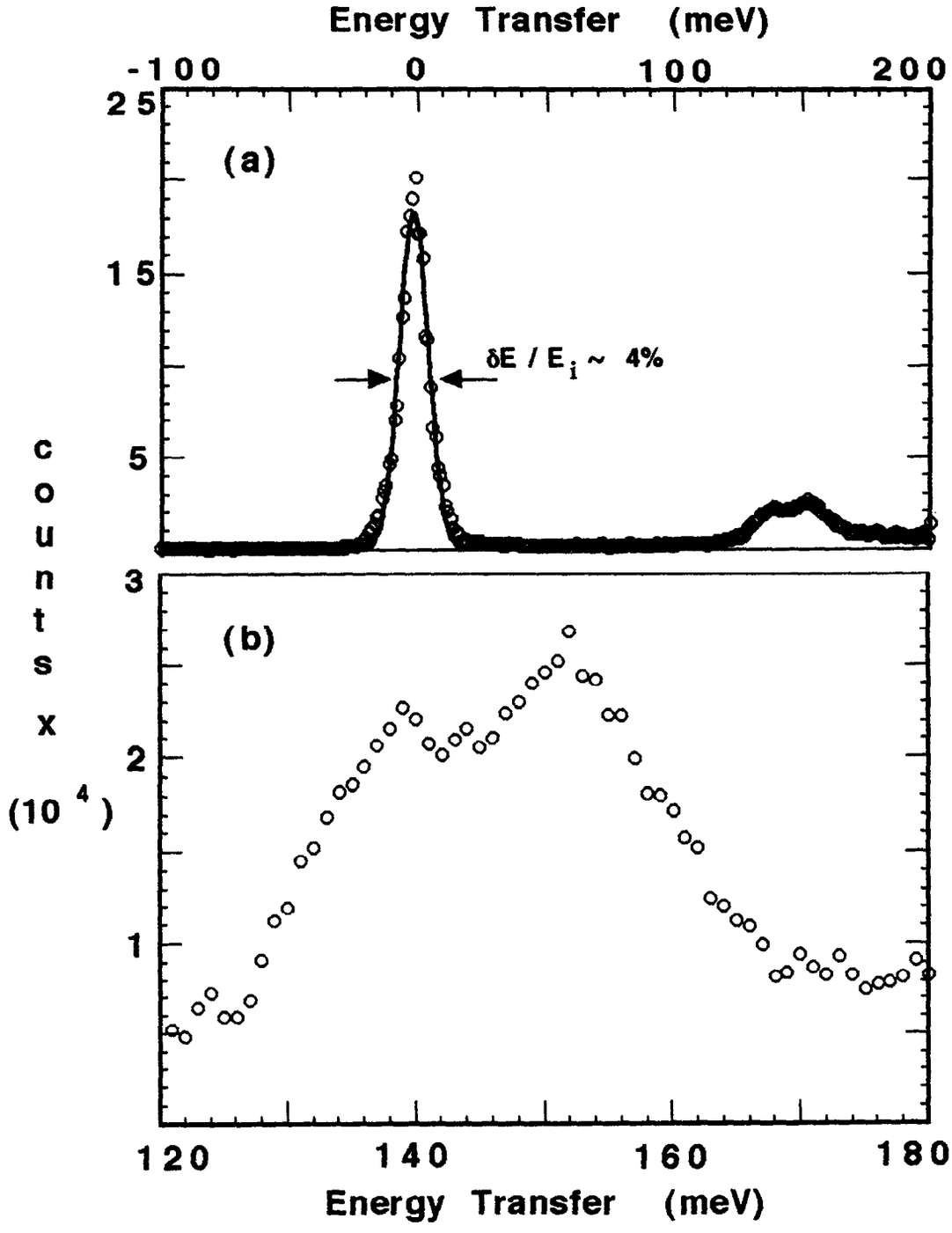
Energy Transfer (meV)
-100
0
100
200
25
15
5
(a)
δE / E_i ~ 4%
counts x (10^4)
3
2
1
(b)
120
140
160
180
Energy Transfer (meV)